

A Coaxial Optrode As Multifunction Write-Read Probe for Optogenetic Studies in Non-Human Primates

Ilker Ozden¹, Jing Wang², Yao Lu³, Travis May¹, Joonhee Lee¹, Werapong Goo⁴, Daniel J. O'Shea⁵, Paul Kalanithi⁶, Ilka Diester^{4,*}, Mohamed Diagne⁷, Karl Deisseroth⁴, Krishna V. Shenoy⁴, Arto V. Nurmikko^{1,2}

¹*School of Engineering, ²Department of Physics, and ³Department of Chemistry, Brown University, Providence, RI, USA*

⁴*Department of Bioengineering, ⁵Stanford Institute for Neuro-Innovation and Translational Neurosciences, Stanford University, Stanford, CA, USA*

⁶*Department of Neurosurgery, Stanford Hospital and Clinics, Stanford, CA, USA*

⁷*Department of Physics, Astronomy and Geophysics, Connecticut College, New London, CT, USA*

**Current address: Ernst Strüngmann Institute, Frankfurt, Germany*

Corresponding Authors:

Arto V. Nurmikko (arto_nurmikko@brown.edu)

Box D, School of Engineering,
Brown University
Providence, Rhode Island 02912, USA
Phone: (401) 863 2869
Fax: (401) 863 9120

Ilker Ozden (ilker_ozden@brown.edu)

Box D, School of Engineering,
Brown University
Providence, Rhode Island 02912, USA
Phone: 001-401-863-1453
Fax: 001-401-863-9120

Highlights:

- Developed powerful new device tool for optogenetic studies in non-human primates
- Multifunction “coaxial optrode” was deployed in non-human primates, rats, and mice
- Device achieved targeted optical stimulation safely with minimal cortical damage.
- Device design and performance correlated well with computational models
- Device was able to quantify and map local opsin expression in the brain

ABSTRACT

Background:

Advances in optogenetics have led to first reports of expression of light-gated ion-channels in non-human primates (NHPs). However, a major obstacle preventing effective application of optogenetics in NHPs and translation to optogenetic therapeutics is the absence of compatible multifunction optoelectronic probes for (1) precision light delivery, (2) low-interference electrophysiology, (3) protein fluorescence detection, and (4) repeated insertion with minimal brain trauma.

New Method:

Here we describe a novel brain probe device, a “coaxial optrode”, designed to minimize brain tissue damage while microfabricated to perform simultaneous electrophysiology, light delivery and fluorescence measurements in the NHP brain. The device consists of a tapered, gold-coated optical fiber inserted in a polyamide tube. A portion of the gold coating is exposed at the fiber tip to allow electrophysiological recordings in addition to light delivery/collection at the tip.

Results:

Coaxial optrode performance was demonstrated by experiments in rodents and NHPs, and characterized by computational models. The device mapped opsin expression in the brain and achieved precisely targeted optical stimulation and electrophysiology with minimal cortical damage.

Comparison with Existing Methods:

Overall, combined electrical, optical and mechanical features of the coaxial optrode allowed a performance for NHP studies which was not possible with previously existing devices.

Conclusions:

Coaxial optrode is currently being used in two NHP laboratories as a major tool to study brain function by inducing light modulated neural activity and behavior. By virtue of its design, the coaxial optrode can be extended for use as a chronic implant and multisite neural stimulation/recording.

Keywords: optogenetics, optoelectronic devices, non-human primates, fluorescence detection, tissue heating, light propagation in tissue

1. Introduction

While optogenetics has rapidly established itself as a powerful tool to study brain function in invertebrates and rodents (Deisseroth, 2011; Yizhar et al., 2011), transition to non-human primates (NHPs) is still at an early stage. Even though robust optical modulation of neural activity has been shown with a variety of optogenetic constructs (Diester et al., 2011; Gerits et al., 2012; Han et al., 2009; Jazayeri et al., 2012), optically-induced behavioral perturbations has been reported only in few studies (Cavanaugh et al., 2012; Gerits et al., 2012; Jazayeri et al., 2012) (also D. J. O et al., 2011 *Soc. Neurosci. Abstr.* 306.11; D. J. O. et al., 2012, *Soc. Neurosci. Abstr.* 208.05; W. G. et al., 2012, *Soc. Neurosci. Abstr.* 229.06). While these results highlight the potential for optogenetics in NHPs to explore the neural substrate of high-level cognitive functions and sensorimotor processing, further development of entirely novel optoelectronic tools is critically required, with capabilities of simultaneous electrophysiological recording, light delivery and fluorescence collection (Gerits et al., 2012) (also D. J. O. et al., 2011 *Soc. Neurosci. Abstr.* 306.11). Advanced NHP studies, especially with chamber-mounted access ports to the brain, typically involve multiple penetrations into the same brain region over weeks and months, thereby demanding probes which are also mechanically robust while minimizing brain damage.

So far, most commonly used probe for optogenetics studies in NHPs has been the “dual-pronged optrode”, based on simply attaching a glass optical fiber to a metal microelectrode (Anikeeva et al., 2012; Diester et al., 2011; Gradinaru et al., 2007). Typically this axially asymmetric construct induces cortical damage after repeated penetrations and presents the additional risk of optical fiber breakage, confounding the interpretation of the observed results. A more recent device, now with axial symmetry, is a glass-coated tungsten electrode (Tamura et al., 2012), designed for usage in NHPs. This probe is formed by four optical fibers embracing a central metal electrode which were subsequently pulled to a sharp tip. Although the device has the interesting feature of delivering or collecting light from four fibers independently, the overall shank diameter (~500 μm diameter) is much larger than a typical microelectrode. It is unclear how durable such a glass-dominated material structure is against multiple penetrations.

Both the dual-pronged-optrode and glass-coated tungsten electrode utilize large diameter optical fibers which limits the optical spatial resolution e.g. in fluorescence imaging. In addition, their optical apertures reside at least few hundred micrometers away from the sites of electrophysiological recording, leading to a non-optimal registry between the site of recording and the spatial profile of both light delivery and fluorescence collection. Thus, optogenetics studies in NHPs would benefit from new types of probes with improved capabilities.

With the motivation for developing a new type of optoelectronic tool for optogenetics in NHPs, here we describe here a “triple-function” coaxial optrode with combined capabilities of electrophysiology, light delivery and fluorescence intensity measurement. The device has a mechanically robust, axially symmetric structure with a diameter comparable to conventional metal microelectrodes enabling multiple penetrations into a targeted brain region with minimal

tissue damage. Its design, informed by computer models, does not impose any constraints on length making it attractive also to studies of deep brain structures. Numerical simulation of electrophysiological recording capabilities gave a priori comparison with conventional metal microelectrodes, while numerical models based on Monte Carlo approaches for photon diffusion (Chow et al., 2010; Wang et al., 2012; Wang et al., 1995) enabled determination of optical energy distribution in the brain tissue - including the safety concerns of heat generation. Quantifying tissue heating and limits on input optical power delivered into the brain have been largely ignored in *in vivo* optogenetics studies. (Optically induced photoelectric artifact effects have been subject to discussion (Long and Fee, 2008; Moser et al., 1993; Yizhar et al., 2011), however minimized in our device during fabrication (**Materials and Methods 2.1**)). While being published elsewhere, ongoing experiments in our laboratories have taken advantage of the capabilities of the new coaxial optrode to generate optically-induced behavioral modulation in NHPs and rodents.

2. Materials and Methods

2.1. Microfabrication of the coaxial optrode

A step-index multimode optical fiber (10/125 μm core/cladding diameters, HPSC10, Thorlabs) (**Supplementary Figure 1(i)**) was cut into a desired length (for our applications $\sim 10\text{-}15$ cm) and tapered at one end by mechanical polishing using a pipette beveler (BV-10, Sutter Instruments) (**Supplementary Figure 1(ii)**) where an 18G stainless steel tube was mounted on the pipette holder (set at $\sim 15\text{-}30^\circ$) to guide the fiber towards the polishing plate. The fiber was rotated continuously in the tube during polishing to obtain a conical tip shape. Following the tapering, the fiber was ultrasonically cleaned in acetone, methanol and water, and an LC miniature connector (MM-FER2007C-1270, OptoEquip) was mounted at the non-tapered end using a heat-curable epoxy (F-123, Thorlabs).

The connectorized and tapered fiber was left in acetone overnight to soften the polymer jacket for easy removal, and sequentially cleaned with acetone and methanol. Next, the fiber was flatly mounted in the electron beam evaporator for deposition of a chromium layer (~ 10 nm) followed by a gold layer ($\sim 100\text{-}300$ nm) (**Supplementary Figure 1(iii)**).

After metallization, the fiber was first inserted into a polyamide tube (~ 3 cm shorter than the fiber, 36AWG, Small Parts) and then into a reinforcing stainless steel tube (29G) (**Supplementary Figure 1(iv)**) which had its end facing the fiber tip chamfered with a drill. At this junction, we followed two different pathways in the fabrication process depending on the purported usage of the optrode. If dura penetration was aimed as in NHPs, the chamfered end was fixed at the start of the tapered segment of the fiber (**Supplementary Figure 1(iv), left**).

Otherwise, the chamfered end was fixed at a desired distance from the tip (**Supplementary Figure 1(iv), right**) to obtain a thinner shank diameter ($\sim 165\ \mu\text{m}$).

Next, UV-curable epoxy (NOA81, Thorlabs Inc.) was manually applied to the tip in 2-3 steps to expose a small portion (semi-conical frustum ($\sim 60^\circ$ opening angle) with top and bottom plane diameters of about $30\ \mu\text{m}$ and $80\ \mu\text{m}$) of the gold coating to the air (**Supplementary Figure 1(v-vi)**) as the recording surface and make a smooth transition from the tapered fiber to polyamide and stainless steel tubes (**Supplementary Figure 1(v)**). Impedance “tuning” ($\sim 100\ \text{k}\Omega$ precision) was accomplished by controlling the amount of exposed metal during dispensing of the epoxy. For electrical contact, a wire (29G) was attached to the metal coating exposed at the connector end of the fiber by using silver epoxy (H20E-PFC, Epoxy Technology). The entire electrical connection pathway was sequentially inserted into a polymer tube for electrical insulation and into a larger stainless steel tube for mechanical rigidity (**Figure 1d**). The tubes were fixed with UV-curable epoxy and entire construct was baked at 60°C overnight for full curing of epoxies.

After the fabrication steps described above, the metal coating partially covered the core of the fiber at the tip where the light exits (**Supplementary Figure 1(v)**). This led to large light induced artifacts (photoelectric effects) (Ayling et al., 2009; Cardin et al., 2010; Han et al., 2009) in the recordings. To minimize these artifacts, we polished the optrode tip perpendicularly on the beveler (**Supplementary Figure 1(vi)**) until the peak-to-peak amplitude of the artifacts induced by 10 ms long laser pulses (10 mW, 473 nm) dropped below $<30\ \mu\text{V}$ within the frequency band from 0.3 to 10 kHz (spike recording regime), where the peak-to-peak noise level in our electrophysiology setup was also $\sim 30\ \mu\text{V}$. As demonstrated by recordings from the posterior parietal cortex of a non-transduced wild-type mouse (**Supplementary Figure 2**), this procedure minimized the amplitude of the artifacts in the spike recording regime to noise level even at the maximum light power ($\sim 16\ \text{mW}$) which could be safely used with the coaxial optrode without critical tissue heating (see section 3.4). However, the artifacts in the frequency range 0.1-250 Hz (local field potential (LFP) recording regime) were still present (**Supplementary Figure 2**). The amplitude and shape of artifacts in the LFP recording varied from experiment to experiment, probably due to their observed dependence on the position of the coaxial optrode in the brain. This caused difficulties in distinguishing neural signals from artifacts in LFP recordings, and therefore, we did not attempt to use the present version of coaxial optrode to monitor LFPs.

2.2. Electrophysiology, Optomodulation Experimental Setup, and Data Analysis

All electrophysiological data was collected with electrode amplifiers (AM-1800, AM Systems interfaced to home-made Labview programs or neural data acquisition unit by Blackrock Microsystems). Data was filtered at 0.3-10 kHz and stored at a computer. All data analysis was performed offline with custom-written programs in Matlab. Tungsten microelectrodes were acquired from MicroProbes (WE30030.5H5) and had a shaft diameter of $125\ \mu\text{m}$.

Optical stimulation was delivered from a blue (473 nm, MLL-III-473) or green (561 nm, MLL-FN-561, Opto Engine LLC) laser and controlled by a Master-8 pulse generator (A.M.P.I.) or a custom made data acquisition system.

2.3. Fluorescence Detection System

The fluorescence detection module accepted fluorescence signals collected through the coaxial optrode. The module operated in a photon counting regime to convert the intensity of fluorescence to a photon count rate. The design of the module (**Supplementary Figure 3**) was based on an epi-fluorescence microscope, where the objective was replaced by the coaxial optrode, i.e. the optrode was used for both delivering light to excite fluorescent molecules and collecting the resulting fluorescence. A relay fiber (10/125 μm core/cladding diameters) connected to the coaxial optrode by an LC-type fiber connector (MM-FER2007C-1270, OptoEquip) was used for guiding both the excitation light to and collect fluorescence signals from the optrode (**Supplementary Figure 3**). The opposite end of the relay fiber was attached to a fiber collimator (F220-SMA, Thorlabs) for coupling the excitation light to and collecting the fluorescence from the relay fiber. The excitation light source was a laser at a wavelength suitable for the excitation of fluorescence molecules of interest, in our case, MLL-III-473 laser (Opto Engine LLC) operating at 473 nm. The excitation and fluorescence collection pathways were separated before the fiber collimator by a dichroic mirror (FF520-Di02-25x36, Semrock). The fluorescence signals emerging from the collimator were guided through this mirror and two sets of emission filters (FF01-542/27-25, Semrock) to a photon counting module (SPCM-AQR-1X, PerkinElmer), an ultrahigh-sensitivity avalanche photodiode (APD) converting each photon to a single short (35 ns) pulse of 2 Volts amplitude. The pulsed output of the APD was converted to a photon count rate by an oscilloscope (TDS2004C, Tektronix). The photon count rate was expected to be proportional to the fluorescence signal level (see below section 2.4), therefore allowing fluorescence intensity to be monitored with high sensitivity.

2.4. Estimation of Opsin Concentration from Fluorescence Signals

At a given position in the brain, the coaxial optrode collects fluorescence signals from local fluorescent molecules and converts them to a single intensity value as a photon count rate. Therefore, for a fixed excitation power, this intensity (or photon count rate) has to be a function of the number, i.e. concentration, of the excited fluorescent proteins. Therefore, the photon count rates could be calibrated to estimate the concentration of fluorescent proteins in the brain. We calibrated the photon count rates using phantom brain preparations (a medium with absorption and scattering properties similar to brain, see below) containing varying concentrations of fluorescein (F6377, Sigma). The relationship between the photon count rate and concentration of fluorescent molecules is shown in **Table 1**.

An interpolation of this data led to a quantitative relationship:

$$r_N = (\text{count rate within the medium})/(\text{count rate outside the medium}) = 1 + 26.5 \cdot c_F (\mu\text{M})^{-1},$$

where r_N is the normalized photon count rate and c_F is the concentration of fluorescent molecules.

Since opsin expression is expected to reside mainly on the neural cell membrane, the concentration calculated with this procedure is an estimate of the average opsin concentration within the optical volume of fluorescence detection.

2.5. Phantom Brain Gel Preparation

60 mg agarose, 2.5 ml of 0.065% TiO_2 , and 1 ml TBE buffer were mixed in 6.5 ml water and the mixture was heated up until boiling while continuously stirring with a magnetic stir bar. Once the heat was turned off, stirring was continued for another 3-5 minutes and a calibrated amount of fluorescent dye was added to reach a targeted concentration of fluorescent molecules in the final gel which had mechanical and optical properties similar to cortical tissue (Yaroslavsky et al., 2002).

2.6. Modeling of the Recording Capabilities of the Coaxial Optrode and the Metal Electrode

In the computational model, the recording device, either a coaxial optrode or a metal electrode, was placed in the center of a cylindrical volume conductor (1 mm radius, 2 mm height) (**Supplementary Figure 4**) having the same electromagnetic properties as homogeneous brain tissue (electrical conductivity $\sigma=0.33$ S/m (Hauelsen et al., 2002)). Our aim was to find the amplitude of the potential generated at the recording device by a point dipole current source, representing a spiking neuron, as a function of its position in the volume conductor. According to Helmholtz reciprocity theorem (Helmholtz, 1853), this computation can be reduced to solving the Poisson equation for the scalar potential generated by a unit current injected through the recording device (Wang, 2012). We solved the corresponding Poisson equation by using COMSOL Multiphysics (COMSOL).

2.7. Monte Carlo Simulations for Characterizing Light Intensity in the Brain

Monte Carlo simulations we employed were based on tracking individual trajectories of many photons as they go through probabilistic scattering and absorption events in the brain after emerging from the fiber aperture (Wang et al., 2012). The brain tissue was considered as a uniformly scattering ($\mu_a=0.07$ mm⁻¹) and absorptive medium ($\mu_s=10$ mm⁻¹) (Yaroslavsky et al., 2002)) with a scattering anisotropy given by the Henyey-Greenstein (HG) phase function:

$$p(\cos\theta) = \frac{1 - g^2}{(1 + g^2 - 2g\cos\theta)^{3/2}}$$

where $p(\cos\theta)d\theta$ is the probability of direction change by an angle θ after a scattering event and $g=0.88$ for the brain (Yaroslavsky et al., 2002). We represented the brain tissue as a 4x4x4 mm³ cube divided into 400x400x400 voxels (voxel size of 10x10x10 μm^3) and the fiber aperture as a

disk at its center. 10^7 photons were launched from this aperture, uniformly distributed across the angle of divergence $\theta_{div} = \sin^{-1}(NA/n_{tissue})$ where NA is the numerical aperture of the fiber and $n_{tissue}=1.36$ is the index of refraction of the brain tissue (Binding et al., 2011). For each photon, a random travel distance, a mean-free-path-step, obeying Beer-Lambert law was generated before any scattering and absorption event. At the end of the step, the weight of existence for the photon was decreased according to the probability of being absorbed. The remaining non-absorbed portion of the photon was redirected again based on the HG phase function. This procedure was repeated for each photon at least 100 times. The outcome of the simulation was the number of photons absorbed at each voxel which could be converted to light intensity at each voxel by

$$\frac{P/10^7}{V \cdot \mu_a} \cdot (\text{number of absorbed photons})$$

where P, V, μ_a and 10^7 are light power from the aperture, volume of a voxel, absorption coefficient and number of launched photons, respectively.

2.8. Tissue Heating and Temperature Rise

To calculate the temperature rise due to absorption of optical energy in the tissue, we numerically solved the Laplace equation for heat diffusion:

$$\rho \cdot c \cdot \frac{\partial T(r, t)}{\partial t} = k \cdot \nabla^2 T(r, t) + p(r, t)$$

where mass density $\rho=1.07 \times 10^6$ g/m³, specific heat capacity $c=3.6$ J/g·K and thermal conductivity $k=0.56$ W/m·K are the material properties of the brain tissue (Holmes, 1998), and T, p, r and t are temperature change, absorbed optical power per volume, space vector coordinate, and time, respectively. To solve this equation numerically, we used the same 3D space unit we defined during Monte Carlo simulations. Accordingly, the absorbed power per volume p was calculated from the absorbed photon counts obtained by Monte Carlo simulation as

$$p = \frac{P/10^7}{V} \cdot (\text{number of absorbed photons})$$

where P and V are the light power and the volume of a voxel, respectively. We performed the numerical calculation with $dt=0.1$ ms time steps (shorter than the diffusion time (~ 0.12 ms) between voxels) by using the recursive relation:

$$T_{x,y,z,n+1} = \frac{\alpha}{6} \cdot (T_{x+1,y,z,n} + T_{x,y+1,z,n} + T_{x,y,z+1,n} + T_{x-1,y,z,n} + T_{x,y-1,z,n} + T_{x,y,z-1,n}) + (1 - \alpha) \cdot T_{x,y,z,n} \\ + \frac{dt}{\rho \cdot c} \cdot p_{x,y,z,n}$$

where x, y, z and n are space and time indices, and

$$\alpha = \frac{6 \cdot k \cdot dt}{\rho \cdot c \cdot ds^2}$$

2.9. Animal Procedures for Rodents and Primates

All rodent procedures were approved by the Brown, and primate procedures by the Brown and Stanford University Institutional Animal Care and Use Committees, respectively, and performed in accordance with the animal welfare guidelines of the National Institutes of Health. The experiments were performed on three animal models: transgenic mice (Thy1-ChR2-YFP (line 18), Jackson Labs) and wild-type rats (Long Evans, Charles River) at Brown, and NHPs (*Macaca mulatta*) at Brown and Stanford. For opsin expression in non-transgenic animals, we used the viral construct AAV5-CamKII α -C1V1(E122T/E162T)-ts-eYFP (4.0×10^{12} genome copies/ml).

Rodent surgeries and experiments were performed under ketamine/xylazine (100/10 mg/kg) or isoflurane (2%) anesthesia. For opsin expression in rats, a small craniotomy (<1 mm) was made above the forelimb area of the motor cortex (2.75/1.25 mm mediolateral/anterior of bregma) and the virus was injected at two depths (0.7 and 1.5 mm from the dura, 1 μ l per injection, 0.1 μ l/min). Following the injections, the craniotomy was closed with bone wax and the skin was sutured. Experiments started at least three weeks after injections. Before experiments, a craniotomy (2-3 mm in diameter) was made above the somatosensory cortex (mice) or forelimb area of the motor cortex (rats), and then the dura was removed throughout the craniotomy.

For NHP work, four adult male monkeys (*Macaca mulatta*) (two at Brown, two at Stanford) were implanted under isoflurane or ketamine/xylazine anesthesia with a recording chamber perpendicular to the skull, in two monkeys over dorsal premotor cortex (upper arm region) and in other two over the somatosensory cortex (hand region). A few weeks after the implantation, 2-3 locations over the cortical region of interest were targeted for injections; and at each location, 1 μ l of virus was injected using an adapted microinfusion system at 1 mm intervals from the cortical surface down to a depth of 5-8 mm. After waiting at least 6 weeks, and before every recording session, (i) either 1 mm length linear incision was made through superficial dura using aseptic technique, and a blunt, non-penetrating guide tube was lowered until resting on the incision site, or (ii) a sharp guide tube was pushed ~0.5-1 mm through the dura and then retracted back to the dura to facilitate optrode penetration into the brain. The coaxial optrode was advanced through the guide tube via a motorized micromanipulator (NaN Instruments).

2.10. Characterization of NHP Tissue Damage

One adult female squirrel monkey (*Saimiri sciureus*) was induced with isoflurane anesthesia in a stereotaxic frame (David Kopf Instruments) and small craniotomies were fashioned bilaterally over sensorimotor cortex. Dura was opened, and the coaxial optrodes and the two-pronged devices, respectively, were mounted on electrode micromanipulators and lowered to 2 mm below cortex onto different nearby cortical targets. After five minutes, the optrodes were withdrawn,

and the animal was euthanized with intravenous pentobarbital and phenytoin and immediately transcardially perfused. Brains were fixed for 10 days in 4% paraformaldehyde and then equilibrated in 30% sucrose in PBS. We cut 40 μ m-thick sections on a freezing microtome and stored them in PBS at 4°C before processing with standard immunohistochemical procedures using the primary antibodies mouse antiNeuN 1:500 (Millipore) in 0.01% Triton X100 and 3% normal donkey serum, secondary antibodies (1:1,000) conjugated to Alexa 647 and DAPI (1:50,000). Confocal fluorescence images were acquired with a high-resolution microscope (Leica).

In addition, 40 μ m-thick histological sections were prepared from one of the rhesus macaques to demonstrate the tissue response after many penetrations with the coaxial optrode into the same brain region.

3. Results

3.1. Design and Fabrication of the Coaxial Optrode

After the numerical model-based design concepts were established, precision microfabrication process flow of the coaxial optrode (**Figure 1a**) began with a tapered inner optical fiber (10/125 μ m core/cladding diameters), half of whose circumference along its length was coated with evaporated 10/100-300 nm thick chromium/gold layers. The fiber was inserted sequentially into a polyamide tube (165 μ m OD) for insulation, and then into a chamfered stainless steel tube (310 μ m OD) for mechanical reinforcement (**Figure 1a**). The chamfered end of the stainless steel tube was kept about 0.1 mm away from the onset of the fiber taper when dura penetration in NHPs was involved. Otherwise, it was retracted back to a desired distance from the tip to allow a thinner shaft diameter (165 μ m) (**Figure 1b**). The structure was fixed together with a biocompatible UV-curing epoxy applied to the tip to ensure a smooth, continuous surface from the tapered tip to the polyamide tube and onto the stainless steel tube. The apex of the tip was polished mechanically to a diameter of about 20-30 μ m to expose the core of the fiber (**Figure 1c**) for maximum light throughput during light delivery/fluorescence collection while minimizing optically induced photoelectric artifacts in electrophysiological recording to the noise level (peak-to-peak amplitude \leq 30 μ V). The impedance values were adjustable to be between 200-600 k Ω by controlling the amount of exposed gold. This impedance range was empirically determined to be optimal for recording from cells across the rodent-primate cross-species range. Details of the fabrication steps and electrical/optical connectorization (**Figure 1d**) are given in **Materials and Methods 2.1**.

We first verified that the coaxial optrode was mechanically robust enough to make multiple penetrations through the dura exposed through chronic recording chambers in NHPs. Due to the flat tip shape of the coaxial optrode, a dimpling of 4-7 mm depth on the brain surface was observed before penetrations (2-5 mm in case of rodents). In rodents, to minimize the amount of dimpling, we simply removed the dura at the insertion site which reduced dimpling to 100-250 μ m. In NHPs, we either used a sharp guide tube or made a 300 μ m linear incision in the dura to

facilitate penetration. To date, we have used four optrodes in two sets of NHP studies. Two optrodes were used for 11 and 13 penetrations (one penetration per recording day) without impairment, i.e. without obvious visible damage on the optrode or significant change in its impedance, respectively, before issues unrelated to the actual optrode performance, such as breakage of the tip or the back-end connections due to mishandling before or after an experiment, terminated the usage of the particular optrodes any further. The other two devices have gone through 19 and 28 penetrations with unimpaired performance and are in active use in behavioral NHP trials at this writing.

3.2. Performance of the Coaxial Optrodes in vivo: Electrophysiology, Optical Modulation and Fluorescence Measurement

As a photonic device, the coaxial optrode was used either for targeted light delivery or for fluorescence measurements by connecting it through a quick-disconnect relay fiber either to a compact solid-state laser (light delivery) or to our compact custom-engineered fluorescence detection module (fluorescence measurement). As an electronic device, even though the design of the coaxial optrode seemed to be potentially suitable for electrical microstimulation, the currents typically used in electrical microstimulation studies were damaging to the coaxial optrode. Therefore, and given the electrochemical liability of gold, we did not investigate electrical microstimulation features of this version of our optrode any further.

To demonstrate and characterize the performance of the coaxial optrode as a triple-function device we performed simultaneous extracellular recording and optical stimulation experiments in (i) transgenic mice (6 animals, Thy1-ChR2/YFP), (ii) transduced rats (3 animals, viral construct AAV5-CamKII α -C1V1(E122T/E162T)-ts-EYFP), and (iii) awake head-fixed transduced rhesus monkeys (4 animals, viral construct AAV5-CamKII α -C1V1(E122T/E162T)-ts-eYFP). In selected cases, we monitored the YFP fluorescence intensity as a function of optrode insertion depth to gauge the opsin expression levels. In the fluorescence collection mode (to improve placement precision and measurement of the opsin expression level), fluorescence protein signals were converted by a compact custom-engineered fluorescence detection module (**Materials and Methods 2.3**) to a photon count rate. This, in turn was calibrated to give an estimate of the concentration of the fluorescent proteins within a given optical volume in the brain.

Figure 2 (top rows) shows experimental examples acquired from somatosensory cortices of the three animal models. In each case the optrode was advanced slowly by microdrives into the brain to collect neural recordings and fluorescence signals at several depths. Light pulses of 500 ms duration were applied (blue and green colored bars) to evoke spiking responses from the recorded cells. Spike waveforms during optically induced and spontaneous activity were identical (**Figure 2**, middle rows) to validate that the recorded neurons were indeed light stimulated. Occasionally, extra spike waveforms could be picked up during stimulation (for example **Figure 2a**, middle row). These may be transients/spikes in the neuropil or spikes from previously silent neurons.

The fluorescence signals collected by the optrode (**Figure 2**, bottom rows) confirmed that the opsin expression at recording locations (indicated by arrows), with estimated average concentrations (see **Materials and Methods 2.4**) of 4.8 μM , 0.1 μM and 0.3 μM for the transgenic mouse, rat and NHP models, respectively. Optical neuromodulation was absent at locations without significant fluorescence signal. For instance, at depths below 1.2 mm in the rat brain (**Figure 2b**, bottom), we were unable to produce optically induced spiking. Overall, the fluorescence signals collected by the coaxial optrode provided useful geographical maps of local opsin expression level. This was further confirmed by comparing the fluorescence intensity profiles obtained to those subsequently obtained from histological sections (**Figure 2a-b**, bottom rows). The comparison showed a good match except for the first 200-250 μm , i.e. the approximate distance the optrode physically displaced the brain surface before entry. The Pearson correlation value between the traces obtained with the optrode and histology was 0.67 ± 0.10 (7 measurements in 3 mice and 1 rat), but increased to 0.83 ± 0.09 when the first 250 μm of the penetration was excluded.

Electrophysiological traces recorded with the coaxial optrode generally consisted of spikes from multiple neurons (**Figure 2**). It was usually easy to isolate individual single units from these traces by using a standard spike-sorting algorithm. The occurrence of spikes from multiple neurons in the recordings is unsurprising considering the shape and size of the exposed metal layer at its tip which forms a sheet on the surface of a semi-conical frustum ($\sim 60^\circ$ opening angle) with top and bottom plane diameters of about 30 μm and 80 μm (**Figure 3c** left column), respectively. As a comparison, metal microelectrodes with similar impedance values ($\sim 500 \text{ k}\Omega$) have conical tips with a height and base diameter of approximately 25 μm and 5 μm , respectively (**Figure 3c** right column). To establish a quantitative comparison between these two structures, we undertook both experiments and numerical model simulations.

In experiments, we performed electrophysiological recordings in the somatosensory cortices of two anesthetized mice with three coaxial optrodes (impedances 400, 500 and 600 $\text{k}\Omega$) and two metal microelectrodes (impedances 500 $\text{k}\Omega$ and 600 $\text{k}\Omega$) concurrently. We advanced their tips 3 mm into the brain while recording spiking data. Our aim was to quantify the average number of recording sites with sortable spike recordings and average spike amplitudes per device. Individual recording sites were determined by using the following procedure: **(1)** as the probe was advanced in the brain, spikes are detected at some locations; **(2)** the probe was further advanced to obtain maximum spike amplitudes; **(3)** electrophysiological data was collected at this point; **(4)** later, using offline analysis, if individual units were determined to be sortable, this location was identified as a recording site; **(5)** after data collection (step (3)), the probe was advanced further until spike amplitudes decreased significantly and/or new spikes emerged; **(6)** the procedure was repeated.

On average, we found 19.7 ± 4.0 (3 penetrations) and 12.3 ± 1.5 (4 penetrations) recording locations per penetration with the microelectrode and optrode, respectively ($p < 0.01$ one-tailed t-

test). As shown in **Figure 3a** (top), 16% of all recordings ($n=49$) with the optrode consisted of spikes from only one cell, 67% from two cells and 16% from at least three cells. By comparison ($p<0.001$, permutation test), 41% of all recordings ($n=59$) with the microelectrode, contained spikes from only one cell, 48% from two cells and 12% from three or more cells (**Figure 3b**)

Next we calculated the mean spike amplitudes for the coaxial optrode and the microelectrode at the recording sites described above in two sets. For the first set, we included only one isolated neuron per recording, choosing the one with the largest spike amplitudes. In this comparison, the median trough-to-peak spike amplitudes were 186 μV (IQR=117-375 μV , $n=59$) and 119 μV (IQR=91-142 μV , $n=49$) for the microelectrode and optrode, respectively ($p<0.001$, one-tailed t-test). In the second set, where all the isolated units are included, the median spike amplitudes were 132 μV (IQR=94-223 μV , $n=101$) and 87 μV (IQR=69-123 μV , $n=94$), respectively ($p<0.001$, one-tailed t-test). The amplitude histograms for the two sets are shown in **Figure 3b**.

In sum, the number of active sites obtained with the optrode per penetration in the cortex was about 62% of that with a metal microelectrode of similar impedance value whereas associated signal amplitudes were about 2.2-2.4 times smaller on average. However, majority of the recorded spikes had comparable amplitudes (see histograms in **Figure 3b**), but large amplitude spikes were more frequent with the metal electrode. Both devices showed similar RMS noise levels of $8 \pm 6 \mu\text{V}$ and $10 \pm 3 \mu\text{V}$ for the coaxial optrode and the metal electrode, respectively. The above comparison from purely electrophysiological point of view is helpful in showing that the current optrode device is practical as a recording device for NHPs – especially when taking into account its other unique assets in the aggregate.

3.3. Electrostatic Modeling of the Coaxial Optrode

We performed first-principles electrostatic modeling to estimate the optrode's spatial recording field in comparison with a metal electrode. The numerical simulations generated maps of signal amplitudes modeled as a unit dipole current source, representing the membrane current during spiking, as a function of its recording site location (see **Materials and Methods 2.6** for the computational model and calculations). The calculated recording fields of the optrode and microelectrode (normalized to the peak amplitude of the optrode recording field) are shown as “heatmaps” in **Figure 3c**. These heatmaps reveal that (i) the ratio of maximum optrode/microelectrode signal is 1/3.58 and (ii) the cortical volume for a given signal amplitude by the optrode is somewhat larger. As complementary view, plots of signal amplitudes versus their corresponding effective volume for both devices (**Figure 3d** (top)) indicate how most recorded spikes originate from neurons located about 10-40 μm away from the sensors and that the effective recording volume of the optrode can exceed that of the microelectrode by about a factor of four (**Figure 3d**, bottom). These results are consistent with experimental observations explaining why the signals are somewhat smaller with the optrode and why these recordings contain spikes from more neurons (note the similarity between **Figure 3d** and histograms in **Figure 3b**).

3.4. Quantifying the Light Delivery from the Coaxial Optrode: Optical Action Volume and Modeling Tissue Heating

Our coaxial optrode has a considerably smaller optical aperture (10 μm diameter, 0.1 NA) than previously used fiber optics or “dual-pronged” optrodes in studies of animal behavior (Anikeeva et al., 2012; Aravanis et al., 2007; Diester et al., 2011; Gerits et al., 2012; Gradinaru et al., 2007; Han et al., 2009; Jazayeri et al., 2012). Since light output distribution, total volume of opsin excitation, and maximum safe in the brain power (determined by tissue heating due to nonspecific absorption of optical power) might depend on aperture size, we estimated these quantities in a model combining Monte Carlo photon diffusion simulations (Chow et al., 2010; Wang et al., 2012; Wang et al., 1995) with heat diffusion dynamics in cortical tissue (**Materials and Methods 2.7 and 2.8**). In general, heat diffusion in the brain is expected to be dependent on the specific local environment of heat generation in the brain due to variations in the local density of brain tissue and blood vessels (which would support heat diffusion). Therefore an exact modeling or precise experimental measurements would be case specific, and beyond the scope of this work. As a generalized case, our simulations assume the brain as a homogenous scattering and absorbing medium and provide a first order approximation to the optically induced heat generation in the brain tissue.

With these simulations, we compared the coaxial optrode to a fiber of 200 μm diameter aperture (0.37 NA) commonly used in reported experimental literature (cited above). First, we calculated iso-intensity contour lines for 10 μm (coaxial optrode) and 200 μm aperture size fibers, respectively, for the same delivered light power of 1 mW (**Figure 4a**). These plots show that the light intensity distribution differs in the immediate proximity of the apertures but converges with distance approximately 100 and 700 μm along the radial and axial directions, respectively. The peak intensities occur at the aperture exit planes scaling approximately inversely proportional to aperture areas. A comparison between intensity levels along the axial direction (**Figure 4b**) shows that the peak intensity for the 10 μm aperture is about 400 times higher than that for the 200 μm aperture, suggesting that the coaxial device might be useful also for nonlinear optical stimulation (e.g. two-photon absorption for spatially selective opsin activation), but that care should be exercised to avoid possible detrimental high optical field effects. In the low power linear regime, we compare in **Figure 4c** the effective opsin excitation volumes for each size of fiber aperture as a function of input light power by normalizing the threshold intensity for opsin activation as 1 mW/mm² (Zhang et al., 2007). These plots show that, for power levels above 0.5 mW, the effective volumes of opsin activation (i.e. number of optically activated cells) are nearly equal for both aperture sizes. However, between 40 and 500 μW , the 200 μm aperture has as much as 2.4 times larger activation volume compared to 10 μm aperture (see inset in **Figure 4c** for low power regime). Below 40 μW , the excitation volume for 200 μm aperture drops virtually to zero whereas there is still opsin excitation possible for 10 μm aperture, showing that the latter is more suitable for minimal excitation applications while being spatially more precise.

Using the numerical simulations for light distribution, we next considered limits to safe light delivery into brain by tissue heating due to absorption of optical energy. First, we calculated spatial maps of initial temperature rise for 10 μm and 200 μm optical apertures in response to a short light impulse (a single square pulse of 1 mW power and 0.1 ms duration, **Materials and Methods 2.8**) (**Figure 5a**). The time scale of the unit impulse is shorter than all thermal time constants in the tissue (**Materials and Methods 2.8**), and thus the optical impulse of energy is completely absorbed before the start of heat diffusion. The temporal dynamics of the temperature distribution in the impulsive limit are plotted as the temperature profile along the axial direction after 10, 20, 30 and 50 ms intervals (**Figure 5b**). These plots show an initial temperature rise for a 10 μm aperture $\Delta T = 1.8 \times 10^{-2} \text{ }^\circ\text{C}$ and, even if a modest value in absolute terms, is much larger than the one for 200 μm aperture ($\Delta T = 6.6 \times 10^{-5} \text{ }^\circ\text{C}$). However, for the smaller aperture heat diffusion is much faster due to the large temperature gradient (**Figure 5a-b**): at about 50 ms following the light impulse the peak temperature in the tissue is virtually identical for both apertures. This impulsive case is useful for understanding the consequences of applying more realistic longer light pulses in optogenetics experiments such as shown in **Figure 5c**. As the heat diffusion is faster for the 10 μm aperture, the temperature rise is now only slightly larger than for the 200 μm aperture case. For example, a light pulse of 1 s duration and 1 mW power is computed to induce a peak temperature rise of $\Delta T = 0.088 \text{ }^\circ\text{C}$ for the 10 μm aperture, i.e. less than 2.5 times the temperature rise for the 200 μm aperture size ($= \Delta T 0.038 \text{ }^\circ\text{C}$) (**Figure 5c**).

To estimate the power levels which can be considered safe for the brain tissue, we assumed that a temperature rise up to 1 $^\circ\text{C}$ is acceptable (Price, 1999). Using this reference for optical case to define the “safe” power limit is meant to provide a guide only as we recognize that the issue is a complex one especially under chronic conditions (and outside the scope of this paper). Our analysis above provides the means to calculate the amount of tissue heating for any temporal patterns of light delivered into the tissue. In recently reported *in vivo* optogenetics studies, many types of temporal patterns are reported (Diester et al., 2011; Gerits et al., 2012; Han et al., 2009; Jazayeri et al., 2012; Tamura et al., 2012; Wang et al., 2011; Wang et al., 2012). Choosing some of these experimental conditions, we determined “safe power limits” for single light pulses of durations up to 1s (**Figure 5d**, top), and for pulse trains (3ms pulse width) delivered at various frequencies for 1s (**Figure 5d**, bottom). By the above criteria, the light levels reported in mentioned literature references and those with our small-aperture coaxial optrode were within the “safe” power regime.

3.5. Assessment of Tissue Damage Caused by the Coaxial Optrode – Histology

Tissue damage was assessed histologically in anesthetized squirrel monkeys as a part of a separate broader study to evaluate various optogenetic constructs (P. K. et al. 2012 *Soc. Neurosci. Abstr.* 229.03). To compare tissue damage caused by insertion, a conventional dual-pronged optrode (250 μm diameter fiber glued to a metal electrode of 75 μm diameter) was used to penetrate motor cortex; a coaxial optrode with a stainless steel tube down to the tip was used

to penetrate the identical spot in contralateral motor cortex. The optrodes were mounted to stereotactic arms and lowered to an identical depth (2 mm below dura). **Figure 6a** shows example of DAPI and NeuN stained sections of the cortex from the penetrated sites. While our aim is not to perform a thorough comparative study of the tissue response to optrodes, as a qualitative description, the damage caused by the dual-pronged optrode (**top rows**) was significant with approximately 200 μm of tissue disruption which appeared like a rupture in the brain tissue. By contrast, the coaxial optrode penetration site displayed no sign of tissue rupture, but a narrow area of disruption of approximately 50 μm . Smaller amount of tissue disruption with the coaxial optrode were anticipated due to its cylindrically symmetric structure, a design which to enable smooth motion through the tissue instead of mechanically rupturing it (which is likely the case for any dual-pronged optrode due to its fork-like tip shape). Our description of the tissue response above was obtained from single-insertion trials in squirrel monkeys. In our experiments with macaques, typically a brain region was penetrated with the optrodes many times day after day leading to accumulated tissue damage which could be much more severe. The histological images in **Figure 6b** shows examples of the amount of tissue disruption caused by the coaxial optrode after more than 30 penetrations in a macaque. The optrode tracks are clearly visible (white arrow) within the somatosensory area which was immune-stained for anti-YFP to track the YFP (co-expressed with C1V1) expression. While we did not characterize the tissue damage in macaques further, this example image shows that after many penetrations the tissue disruption is still considerably milder than the one observed with dual-pronged optrodes.

From another perspective, the dual-pronged optrodes was subject to breaking during insertion into the brain due to the blunt tip of the fiber, even if a guide tube was used for dura penetration, leaving a broken piece of fiber in the brain. This adds up an extra level of difficulty in its applicability to NHP studies by contributing to the amount of brain damage and decreasing the reliability of the experiments. In our experience with the coaxial optrode so far, we have never encountered a breakage. Thus the histological observations and structural properties of the probes support the observed electrophysiological evidence that our coaxial optrode enables a vastly safer means for performing light delivery and electrophysiological recordings in the primate model, when compared with commonly used segmented dual-pronged and similar devices.

4. Discussion

In this report, we have described the design, microfabrication and performance of the new coaxial optrode as a triple-function optical/electrical probe, specifically overcoming major obstacle in advancing optogenetics research in NHPs. We have shown through experiment and models that the device has reached the level of practical utility to advance optogenetic NHP studies, perhaps providing a reliable standard for the research community. The coaxial optrode offers significant advantages over earlier devices, e.g. the dual pronged-optrode and glass-coated tungsten electrode recently used in NHP optogenetics studies. We have demonstrated that the

mechanically robust and axially symmetric structure of the coaxial optrode allows multiple penetrations into the primate brain with minimal tissue damage. Its design, including the small optical aperture ($\sim 10\ \mu\text{m}$) is well suited for precision targeting and spatial distribution of light delivery (**Figure 4b-c**) at resolution not possible with earlier probes. The illuminated brain volume is spatially more closely co-registered with simultaneous read-out electrophysiology. The coaxial device brings the advantage of higher degree of confidence in locating of the target brain regions while determining the levels of opsin expression. In the experiments presented in this report, recordings and light delivery/collection were performed down to 2 mm in the brain since the focus of our studies was the cortex. However, the design and physical characteristics of the coaxial optrode will readily allow spatially precise studies in targeted deeper brain structures, with minimal brain damage, including a chronic version of the device. Finally we note that the device is scalable in that it should be practical to deploy several optrodes together for simultaneous multisite electrophysiology and spatio-temporally controlled patterned illumination.

Furthermore, the small optical aperture size does not limit the spatial extent of opsin excitation (**Figure 4c**), or exclude affecting behavioral modulation. For example, we were able to generate visible muscle twitch responses in rodents using light power levels below 3 mW from the coaxial optrode (data not shown). In the case of NHPs, the current coaxial optrode is being used in ongoing studies of O'Shea, Goo, et al (D. J. O. al., 2011 *Soc. Neurosci. Abstr.* 306.11; D. J. O. et al., 2012, *Soc. Neurosci. Abstr.* 208.05; W. G. et al., 2012, *Soc. Neurosci. Abstr.* 229.06), where light delivery at 1-3 mW level input powers to dorsal premotor cortex has enabled comparison of behavioral and electrophysiological outcomes (data not shown, results to be reported). Finally, we note that the electrophysiological responsivity of the coaxial optrode can be finessed via microfabrication such as gold-coating smaller fractions of the fiber surface and/or multi-segmenting the metallization, analogous to a tetrode for enhanced single-unit isolation and larger signals.

Acknowledgements

We thank Ying-Ping Liu for expertise with the fabrication of coaxial optrodes, Tasha Nagamine for assistance with the construction of the fluorescence detection module, David Sheinberg, Valerie Yorgan, Ji Dai and Daniel Brooks for their help and suggestions throughout the development of the optrode, and the Donoghue Lab for expertise with NHPs. The work at Brown was supported by DARPA REPAIR (N66001-10-C-2010) and (rodent work by) NSF/EFRI grants. The work at Stanford was supported by DARPA REPAIR (N66001-10-C-2010) and NIH Director's Pioneer Award (1DP1OD006409) grants.

REFERENCES

- Anikeeva P, Andalman AS, Witten I, Warden M, Goshen I, Grosenick L, Gunaydin LA, Frank LM, Deisseroth K. Optetrode: a multichannel readout for optogenetic control in freely moving mice. *Nat Neurosci*, 2012; 15: 163-70.
- Aravanis AM, Wang LP, Zhang F, Meltzer LA, Mogri MZ, Schneider MB, Deisseroth K. An optical neural interface: in vivo control of rodent motor cortex with integrated fiberoptic and optogenetic technology. *J Neural Eng*, 2007; 4: S143-56.
- Ayling OG, Harrison TC, Boyd JD, Goroshkov A, Murphy TH. Automated light-based mapping of motor cortex by photoactivation of channelrhodopsin-2 transgenic mice. *Nat Methods*, 2009; 6: 219-24.
- Binding J, Ben Arous J, Leger JF, Gigan S, Boccara C, Bourdieu L. Brain refractive index measured in vivo with high-NA defocus-corrected full-field OCT and consequences for two-photon microscopy. *Opt Express*, 2011; 19: 4833-47.
- Cardin JA, Carlen M, Meletis K, Knoblich U, Zhang F, Deisseroth K, Tsai LH, Moore CI. Targeted optogenetic stimulation and recording of neurons in vivo using cell-type-specific expression of Channelrhodopsin-2. *Nat Protoc*, 2010; 5: 247-54.
- Cavanaugh J, Monosov IE, McAlonan K, Berman R, Smith MK, Cao V, Wang KH, Boyden ES, Wurtz RH. Optogenetic inactivation modifies monkey visuomotor behavior. *Neuron*, 2012; 76: 901-7.
- Chow BY, Han X, Dobry AS, Qian X, Chuong AS, Li M, Henninger MA, Belfort GM, Lin Y, Monahan PE, Boyden ES. High-performance genetically targetable optical neural silencing by light-driven proton pumps. *Nature*, 2010; 463: 98-102.
- Deisseroth K. Optogenetics. *Nat Methods*, 2011; 8: 26-9.
- Diester I, Kaufman MT, Mogri M, Pashaie R, Goo W, Yizhar O, Ramakrishnan C, Deisseroth K, Shenoy KV. An optogenetic toolbox designed for primates. *Nat Neurosci*, 2011; 14: 387-97.
- Gerits A, Farivar R, Rosen BR, Wald LL, Boyden ES, Vanduffel W. Optogenetically Induced Behavioral and Functional Network Changes in Primates. *Curr Biol*, 2012.
- Gradinaru V, Thompson KR, Zhang F, Mogri M, Kay K, Schneider MB, Deisseroth K. Targeting and readout strategies for fast optical neural control in vitro and in vivo. *J Neurosci*, 2007; 27: 14231-8.
- Han X, Qian X, Bernstein JG, Zhou HH, Franzesi GT, Stern P, Bronson RT, Graybiel AM, Desimone R, Boyden ES. Millisecond-timescale optical control of neural dynamics in the nonhuman primate brain. *Neuron*, 2009; 62: 191-8.
- Haueisen J, Tuch DS, Ramon C, Schimpf PH, Wedeen VJ, George JS, Belliveau JW. The influence of brain tissue anisotropy on human EEG and MEG. *Neuroimage*, 2002; 15: 159-66.
- Helmholtz H. Über einige Gesetze der Vertheilung elektrischer Ströme in körperlichen Leitern mit Anwendung auf die thierisch-elektrischen Versuche. *Ann. Physik und Chemie*, 1853; 89: 354-77.
- Holmes KR. Thermal conductivity of selected tissues. In Diller KR, editor. *Biotransport: Heat and Mass Transfer in Living Systems*. New York Academy of Science: New York, 1998.
- Jazayeri M, Lindbloom-Brown Z, Horwitz GD. Saccadic eye movements evoked by optogenetic activation of primate V1. *Nat Neurosci*, 2012.
- Long MA, Fee MS. Using temperature to analyse temporal dynamics in the songbird motor pathway. *Nature*, 2008; 456: 189-94.
- Moser E, Mathiesen I, Andersen P. Association between brain temperature and dentate field potentials in exploring and swimming rats. *Science*, 1993; 259: 1324-6.
- Price RR. The AAPM/RSNA physics tutorial for residents. MR imaging safety considerations. *Radiological Society of North America. Radiographics*, 1999; 19: 1641-51.
- Tamura K, Ohashi Y, Tsubota T, Takeuchi D, Hirabayashi T, Yaguchi M, Matsuyama M, Sekine T, Miyashita Y. A glass-coated tungsten microelectrode enclosing optical fibers for optogenetic exploration in primate deep brain structures. *J Neurosci Methods*, 2012; 211: 49-57.

Wang J. Combined Optical Stimulation and Neural Recording in In Vivo Neuromodulation. PhD Dissertation, Brown University, 2012.

Wang J, Ozden I, Diagne M, Wagner F, Borton D, Brush B, Agha N, Burwell R, Sheinberg D, Diester I, Deisseroth K, Nurmikko A. Approaches to optical neuromodulation from rodents to non-human primates by integrated optoelectronic devices. *Conf Proc IEEE Eng Med Biol Soc*, 2011; 2011: 7525-8.

Wang J, Wagner F, Borton DA, Zhang J, Ozden I, Burwell RD, Nurmikko AV, van Wagenen R, Diester I, Deisseroth K. Integrated device for combined optical neuromodulation and electrical recording for chronic in vivo applications. *J Neural Eng*, 2012; 9: 016001.

Wang L, Jacques SL, Zheng L. MCML--Monte Carlo modeling of light transport in multi-layered tissues. *Comput Methods Programs Biomed*, 1995; 47: 131-46.

Yaroslavsky AN, Schulze PC, Yaroslavsky IV, Schober R, Ulrich F, Schwarzmaier HJ. Optical properties of selected native and coagulated human brain tissues in vitro in the visible and near infrared spectral range. *Phys Med Biol*, 2002; 47: 2059-73.

Yizhar O, Fenno LE, Davidson TJ, Mogri M, Deisseroth K. Optogenetics in neural systems. *Neuron*, 2011; 71: 9-34.

Zhang F, Wang LP, Brauner M, Liewald JF, Kay K, Watzke N, Wood PG, Bamberg E, Nagel G, Gottschalk A, Deisseroth K. Multimodal fast optical interrogation of neural circuitry. *Nature*, 2007; 446: 633-9.

FIGURE LEGENDS

Figure 1. The structure of the coaxial optrode. (a) Cross sectional schematic (**top**) and side view photograph (**bottom**) of the coaxial optrode showing main constituent parts. The center optical fiber has a 10 μm diameter optical aperture (exposed core of the fiber) leading to highly directional light output as visualized in dye-doped saline. The saline contains $\sim 1 \mu\text{M}$ fluorescein with fluorescence excited by 473 nm laser light (**bottom**). (b) A larger scale image of the device where the reinforcing thin stainless steel jacket (310 μm outer diameter) was kept few centimeters away from the tip leading to a thinner tissue penetrating portion of the shaft (diameter 165 μm). (c) Scanning electron microscope images of the coaxial optrode tip. The tip was polished to a flat circular tip of diameter 20-30 μm to separate the optical aperture from the surrounding gold recording electrode layer. This design reduced light-induced artifacts in the electrophysiological recordings to noise level. (d) Full length photograph of the coaxial optrode showing its electrical and optical connections at the distal end.

Figure 2. In vivo performance of the coaxial optrode. (a-c) Demonstrating the triple-functionality of the device in (a) an anesthetized mouse (transgenic Thy1-ChR2/YFP), (b) anesthetized rat (transduced with AAV5-CAMKII α -C1V1-eYFP), and (c) awake behaving non-human primate (transduced with AAV5-CAMKII α -C1V1-eYFP). The **top panels** in (a-c) show examples of optically modulated electrophysiological recordings from somatosensory cortices with blue and green bars indicating periods of light delivery (at 473 nm for the mouse and 561 nm for the rat and NHP cases, respectively). The recordings were acquired at depths indicated by arrows in the **bottom panels**. Light-induced increase in spiking activity is clearly visible in all

recordings. The spike shapes of the isolated neurons (black and red traces in **middle panels**) were indistinguishable during spontaneous and optically-stimulated periods indicating that the activity of the recorded neurons was modulated by light. In case of the transgenic mouse, optical stimulation evoked spiking from another nearby neuron which was otherwise silent (column **a**, **middle panel**). The **bottom panels (a-c, solid lines)** show the fluorescence signal amplitudes (from YFP) collected as the device was advanced into the brain during the recording sessions (at 50 μm and 250 μm intervals in case of rodents and NHP, respectively). The fluorescence amplitudes were expressed as logarithm of the fluorescence intensity normalized to its value outside the brain. For comparison, fluorescence intensity profiles from histological sections (**a-b**, **bottom right panels**) at the sites of penetration are plotted as dashed lines. Except for the initial 200 μm distance from the dura, fluorescence profiles obtained from the coaxial optrode and histology were similar. The cortical layers are indicated with roman numbers to demonstrate the capability of the optrode to detect layer specific expression level. (Histological YFP fluorescence characterization was not performed in the case of the primates; see, however, Figure 6 related to NHP histology). Also note that although the viral injections in rats and NHPs were made at discrete targeted locations, the injection sites were not clearly tractable from the histological and fluorescence collection data since, under our injection conditions, the AAV-based gene delivery at a single site leads to a uniform gene expression within a region of radius more than 1 mm in the tissue, thereby averaging out any clear indication of individual injection sites.

Figure 3. Assessing electrophysiological recording capabilities of the coaxial optrode in comparison to a metal microelectrode (similar impedance value). (**a-b**) Experimental comparison of the recording capabilities for the two devices. (**a**) The distribution of the number of identified neurons per recording for the coaxial optrode and metal electrode. (**b**) Distribution of spike amplitudes (**top** for the coaxial optrode, **bottom** for the metal electrode) when only the average spike-amplitudes of neurons with largest spikes at each recording were considered (**left column**), and when the average spike-amplitudes of all isolated neurons were considered (**right column**). (**c-d**) Comparison through numerical modeling of the recording capabilities of the two devices. (**c**) The spatial profiles of signal amplitudes recordable by the coaxial optrode (**left column**) and the metal electrode (**right column**) are shown as “heatmaps”. The maps in the top rows show the recorded field profiles projected on the plane in which the devices lie, whereas the bottom rows project the amplitude contours onto the perpendicular plane (indicated by dashed lines in the top rows). Note that color code scale for the coaxial optrode is about 3.58 times smaller than the one for the metal electrode. (**d**) The signal amplitudes for the coaxial optrode and metal electrode vs. the cube-root of the modeled volume (**top**). For better visualization, the volume is converted to “distance” by taking its cube-root. The ratio of recording volume for the coaxial optrode to that for the metal electrode for each chosen signal amplitude (**bottom**).

Figure 4. Numerical modeling of the light output pattern for the coaxial optrode (10 μm optical aperture) in comparison to a flat optical fiber (200 μm optical aperture). (**a**) Intensity distributions for a total output power of 1 mW from the coaxial optrode (**left**) and the

larger aperture fiber (**right**). The iso-intensity curves were obtained by Monte Carlo simulations applied to a homogenous medium with absorptive and scattering properties those of cortex. **(b)** Intensity profiles along the axial (z) propagation direction. **(c)** Dependence of the effective volumes of opsin excitation on optical power assuming 1 mW/mm^2 as sufficient intensity to exceed excitation threshold for opsin expressing neurons (blue and red dashed curves for the coaxial optrode and fiber, respectively). The inset plot shows the excitation volumes at low power regime.

Figure 5. Tissue heating when comparing the coaxial optrode (10 μm optical aperture) with flat optical fiber (200 μm optical aperture). **(a)** Maps of temperature rise in tissue in response to a 1 mW light pulse of 0.1 ms “impulse” delivered through the coaxial optrode (**left**) and the fiber (**right**). **(b)** The temperature rise profile along the axial (z) direction following the light impulse (**left** for the coaxial optrode, **right** for the fiber). The curves with different colors correspond to different times after the light impulse. **(c)** The dependence of the temperature rise to representative experimental pulse durations up to 1 s. The cooling of the tissue by diffusive transport is evident in portions of the curves after 1 s (x-axis). **(d)** The dependence of the estimated safe power levels on optical pulse duration (**top**) and frequency (**bottom**). The frequency calculations were made by assuming that each optical event was 3 ms long and applied as a pulse train at the specified frequencies for 1 s. The safe power levels were calculated by assuming that 1°C rise in temperature is acceptable (from regulations by FDA on RF energy deposition generated during MRI). The safe power limits were 11.4 mW and 26.3 mW for 10 μm and 200 μm apertures, respectively, for a light pulse of 1 s duration. In case of trains of light pulses, few selections were 20.4 mW and 408.8 mW for 10 Hz, 19.0 mW and 154.6 mW for 100 Hz, and 13.1 mW and 34.9 mW for 250 Hz for 10 μm and 200 μm apertures, respectively.

Figure 6. Comparison of brain tissue damage induced by the coaxial and dual-pronged optrodes after penetrations. **(a)** Upper images are from dual-pronged optrode insertion. Lower images are from coaxial optrode insertion. Images on the left display tissue stained with 4',6-diamidino-2-phenylindole (DAPI), a non-specific marker for DNA. Images on the right display tissue stained with NeuN, a marker for neurons. **(b)** Histological images (low and high magnification at the top and bottom, respectively) of the somatosensory cortex from a macaque. The dark regions are where the opsin C1V1 is expressed as revealed by anti-YFP immunostaining. This region was penetrated more than 30 times with the coaxial optrode over a six months period. The optrode tracks are indicated by white arrows. The full tracks are not visible in these images since the coronal histological sections were not parallel to the optrode track.

Table 1: Fluorescein concentration vs corresponding normalized photon count rate.

c_F=concentration of fluorescein (μM)	r_N= count rate within the medium/count rate outside the medium
0	1
0.1	3.78
1	28.81
10	252

Figure 1
[Click here to download high resolution image](#)

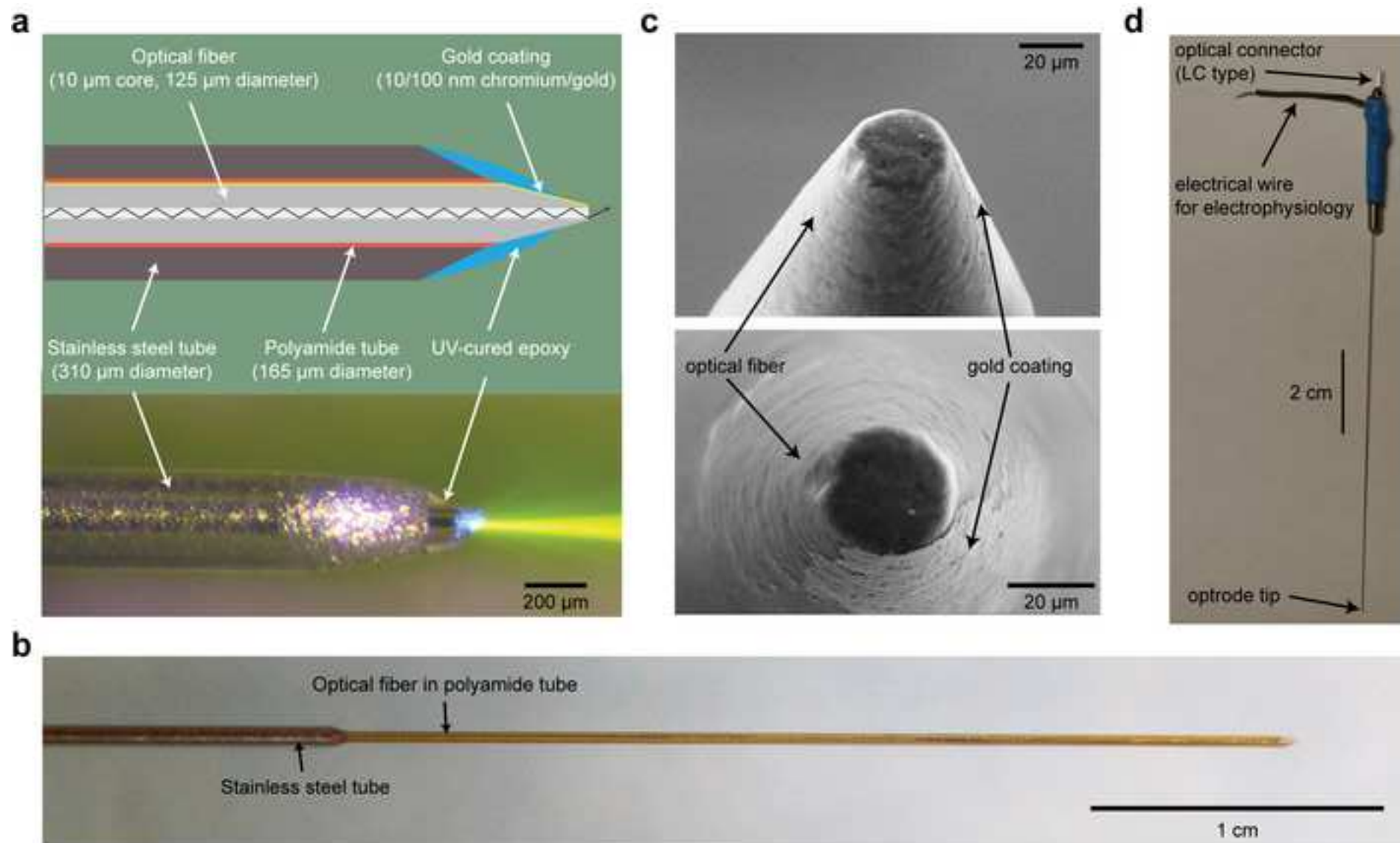


Figure 1
 Ozden et al.

Figure 2
[Click here to download high resolution image](#)

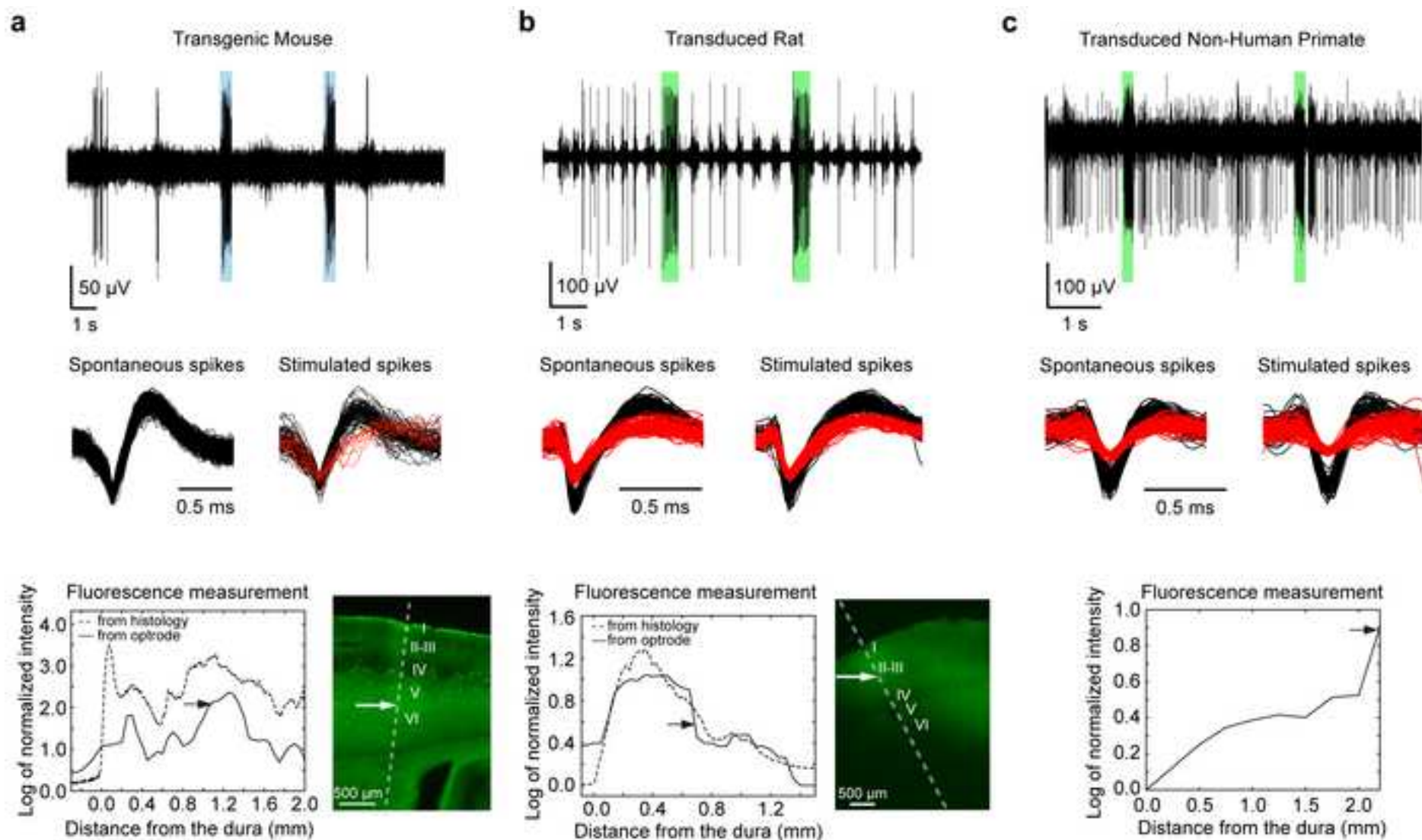


Figure 2
 Ozden et al.

Figure 3
[Click here to download high resolution image](#)

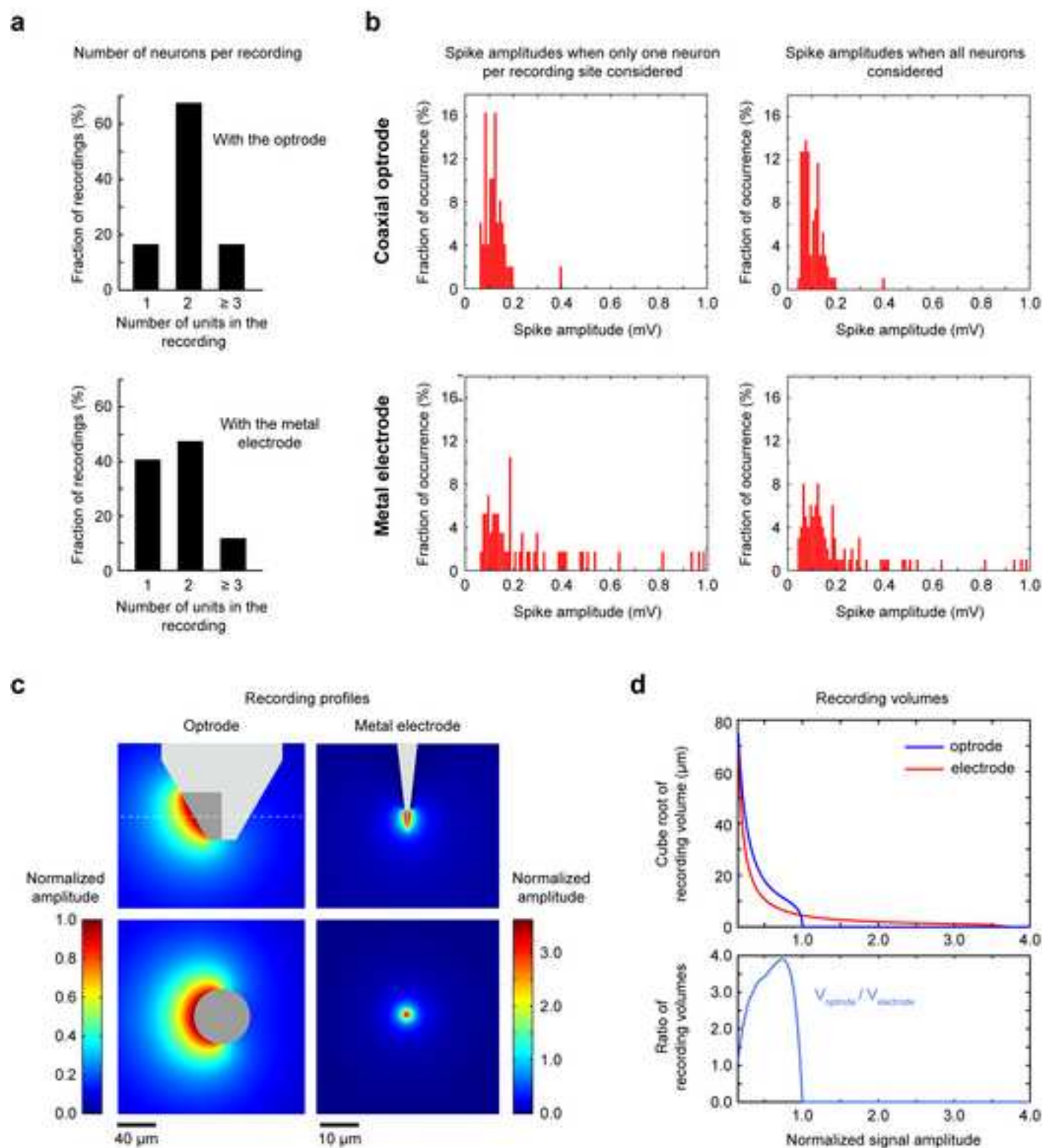


Figure 3
 Ozden et al.

Figure 4
[Click here to download high resolution image](#)

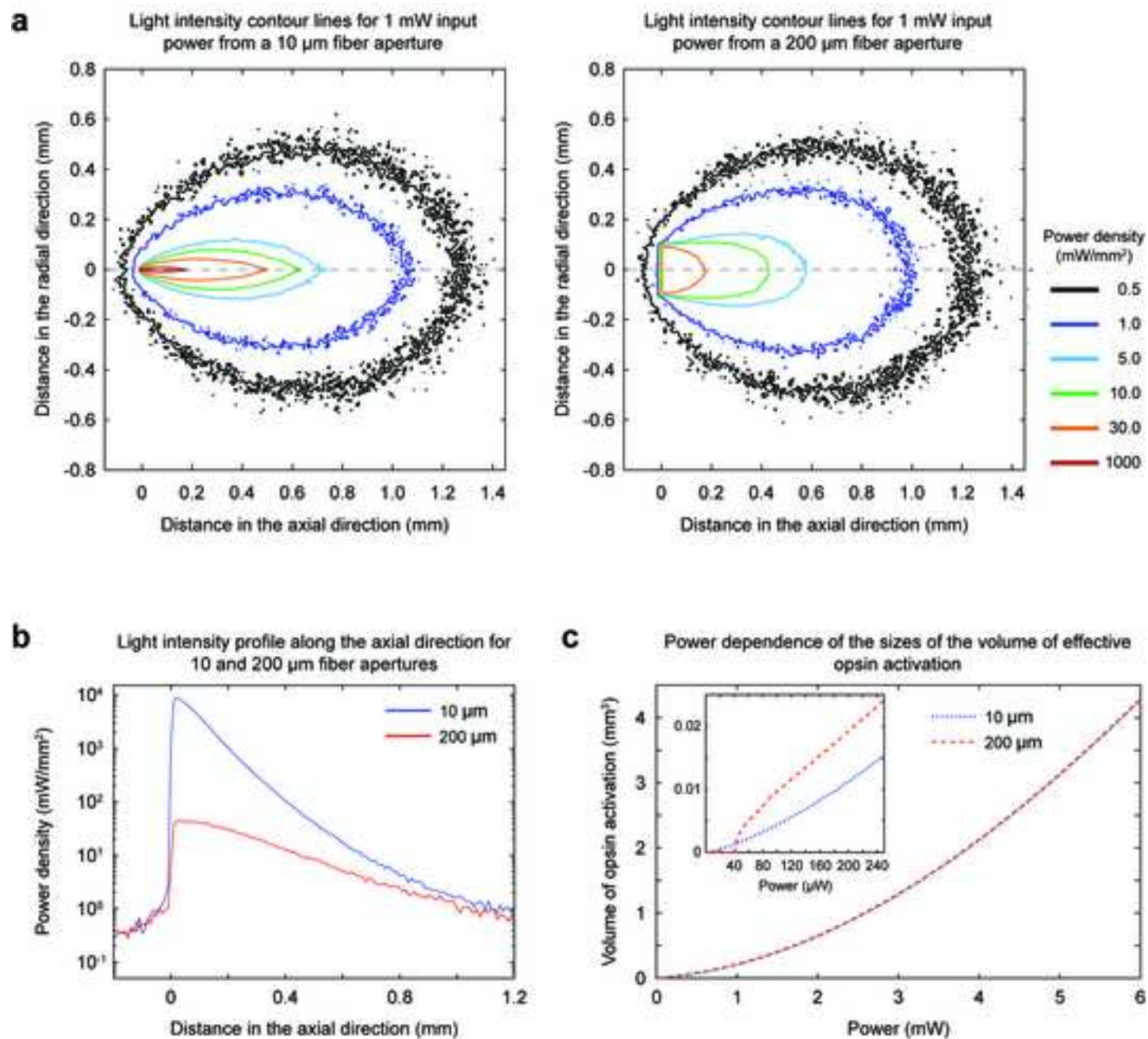


Figure 4
 Ozden et al.

Figure 5
[Click here to download high resolution image](#)

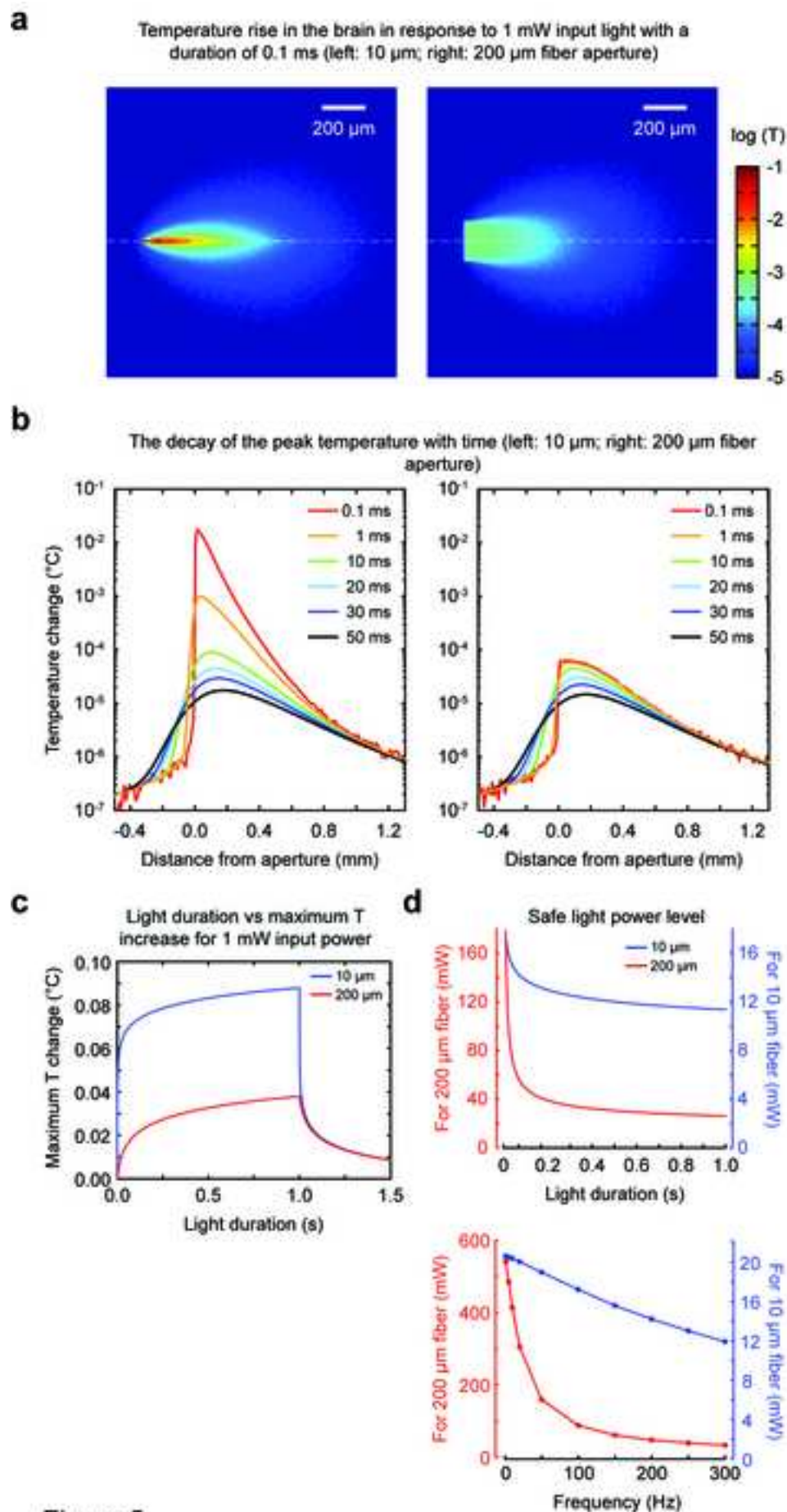
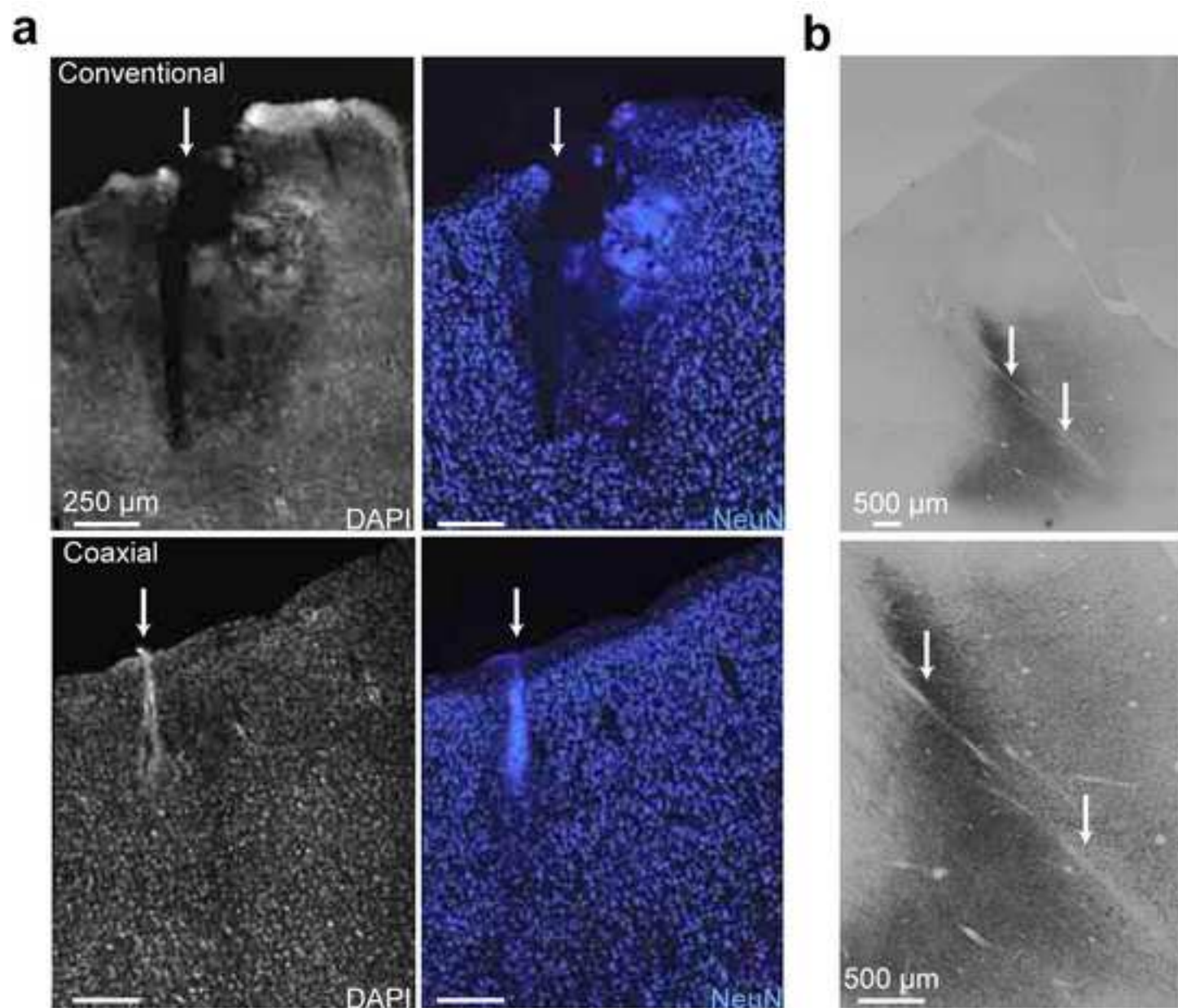
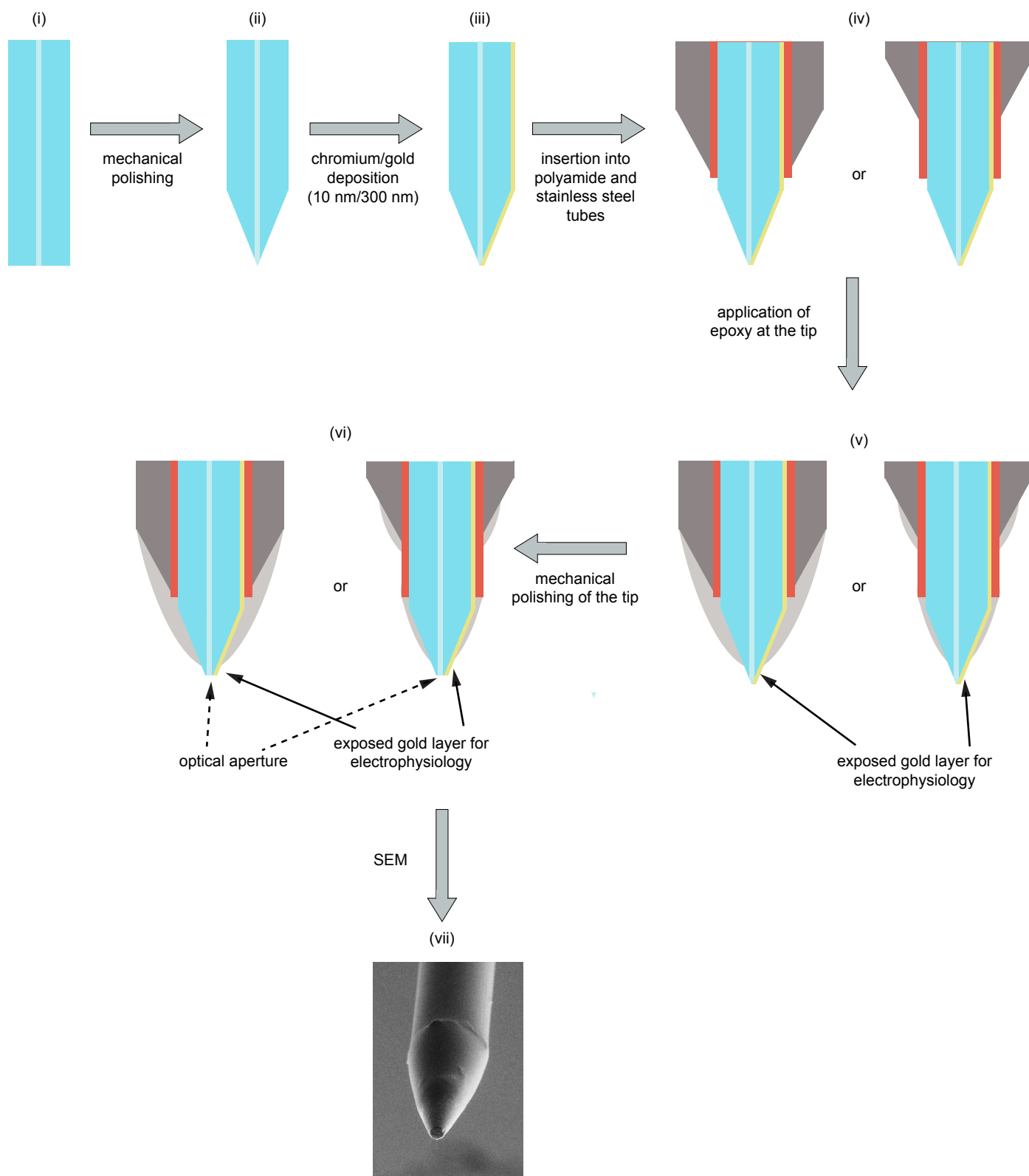


Figure 5
 Ozden et al.

Figure 6
[Click here to download high resolution image](#)



Ozden et al.
Figure 6



Supplementary Figure 1
Ozden et al.

Single trial within 0.3-10 kHz

Average within 0.3-10 kHz
(50 trials)

Average within 0.1-250 Hz
(50 trials)

0.7 mW



30 μ V

200 ms

2 mW



10 mW

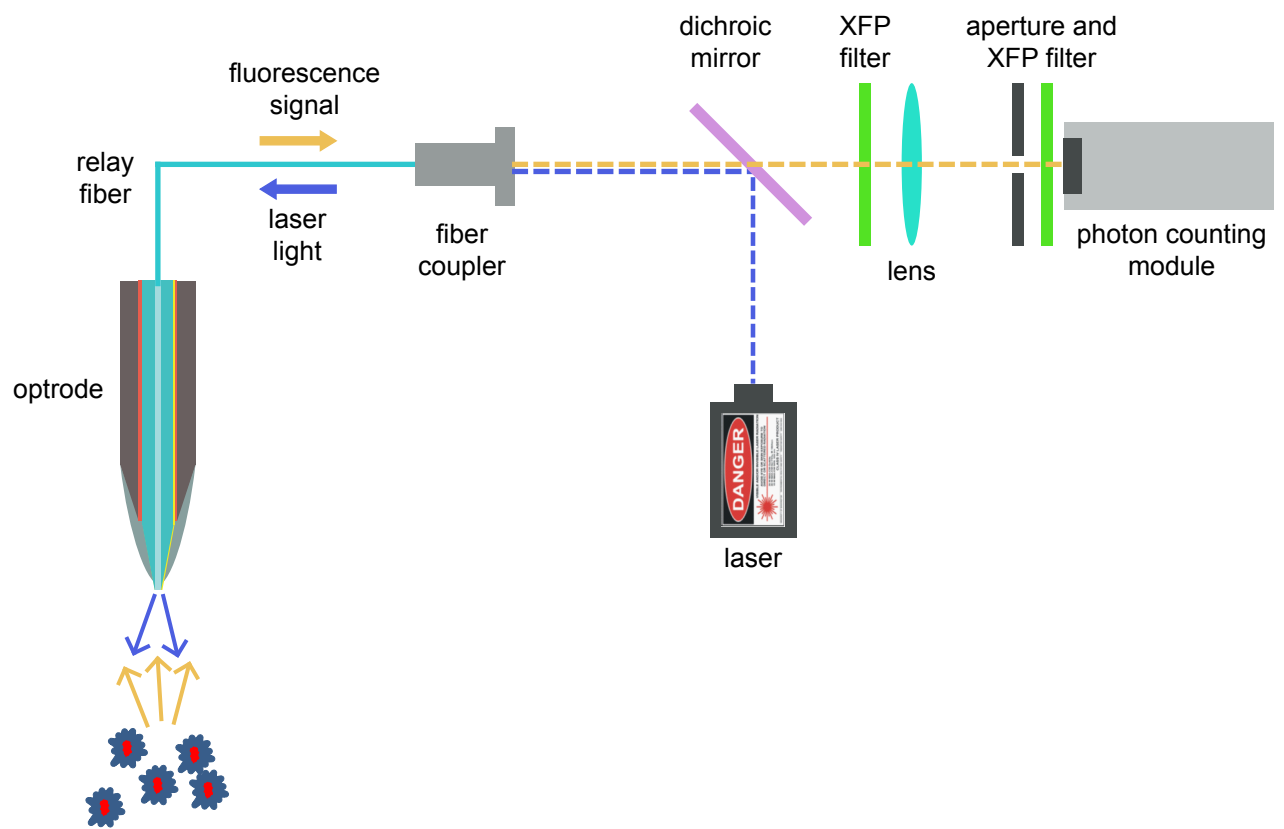


45 mW

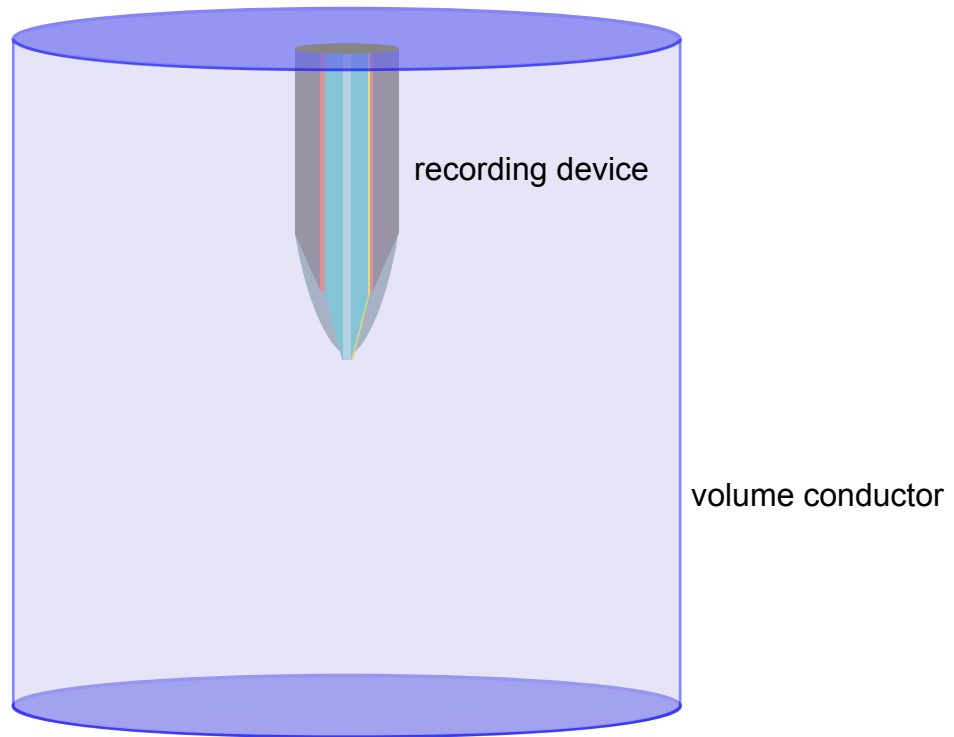


1 ms

Supplementary Figure 2
Ozden et al.



Supplementary Figure 3
Ozden et al.



Supplementary Figure 4
Ozden et al.